

Award Accounts

The Chemical Society of Japan Award for Creative Work for 2009

Development of Multivalent Ion Conducting Solid Electrolytes

Nobuhito Imanaka* and Shinji Tamura

Department of Applied Chemistry, Faculty of Engineering, Osaka University, 2-1 Yamadaoka, Suita, Osaka 565-0871

Received July 1, 2010; E-mail: imanaka@chem.eng.osaka-u.ac.jp

Trivalent cation conduction has been successfully demonstrated by two strategies. One is crystal structure selection, and the other is the selection of the constituent ions in solids. Since the trivalent cations possess certain ionic volume, a suitable mobile ion pathway should appear in the structure. One candidate structure we selected is a two-dimensional layered structure and the other is a three-dimensional network crystal structure. The selection of the constituent ions in solids is performed by considering the electrostatic interaction between cations and anions in the structure.

1. Introduction

It has been long known that the mobile species in solids is electrons or holes as can be easily seen in metals and semiconductors. In contrast, there are unique solids in which the mobile species are only ions and these are called ionic conducting solids (Solid electrolytes).

As early as the end of the 19th century, the relationship between electric current and chemical change in solids was found to obey Faraday's law.[1] Stabilized zirconia, one of the most well-known solid electrolytes (ionic conducting solids), was first realized as a light source in 1897, by the application of resistive-heating, and was known as a Nernst glower (Here, zirconia means zirconium dioxide and "stabilized" indicates that the high-temperature phase is stabilized by replacing tetravalent zirconium ion site with aliovalent cation.). Nernst was the inventor of the glower and he suggested that the electric current in the device came by the flow of oxide anions in stabilized zirconia. At present, stabilized zirconia has been widely applied as a component of oxygen sensors. A more comprehensive understanding of electrical conduction in such ionic conducting solids was devoloped in a thesis by Wagner in 1943.[2]

In the course of research on solid electrolytes, there are three outstanding representative milestones. First is the extraordinary high ion conductivity found in silver iodide (AgI) by Tubandt et al. in 1921.[3] The Ag^+ ion conductivity in the α-phase that forms at temperatures higher than 149 °C approaches that of molten salts and the ion conductivity exceeds the conductivity of aqueous NaCl solution at room temperature. Second is β-alumina ($Na_2O \cdot 11Al_2O_3$) possessing layered structure with Na^+ ion conduction appearing between the layers. Third is the development of NASICON (Na^+ super ionic conductors; $Na_{1+x}Zr_2P_{3-x}Si_xO_{12}$), which was designed and prepared by Goodenough et al. in 1976 in order to obtain high ionic conduction in solids.[4] NASICON is formed by tetrahedral SiO_4 and PO_4, and also hexagonal ZrO_6 polyhedra, by linking the oxide ions to form three-dimensional network structure, which is suitable for ion migration.

As can be seen in the chronology of solid-state ionics described above, the mobile ion species are mainly monovalent or divalent ions and it is clear that the ion conduction in solids mainly depends on the valence of the conducting ionic species. In the case of trivalent or higher valent ions, they have been long believed to be extremely poor migrants in solids due to high electrostatic interaction between the conducting ion and the counter ion species in the solids. Therefore, the migrating ion species in solids was believed to be limited to certain mono- and divalent ions until 1995.

2. Strategy—Development—

By consideration of the following three key issues, multivalent ion conduction in solids has been realized.

1) Substitute trivalent cation sites partially with tetra-, penta-, and/or hexavalent cations: Since electrostatic interaction depends on the constituent elements, it is expected to reduce the interaction between trivalent cation and the constituent counter anion such as oxide anion, by partially replacing the trivalent sites with tetra-, penta-, or hexavalent cations. By reduction of interaction, trivalent cations are able to migrate more smoothly than before substitution (In the case of alumina (Al_2O_3), composed of trivalent aluminum cations and oxide anions, the cations and the anions strongly bind by electrostatic interaction, hence the trivalent aluminum ions cannot migrate in the solid at all.).

2) Select structures where bulky multivalent cations can migrate inside the crystal structure: One is layered two-dimensional structures such as β-alumina and the other is three-dimensional network structures, like NASICON as described above.

Published on the web March 11, 2011; doi:10.1246/bcsj.20100178

3) Avoid the inclusion of mono- or divalent cations in solids: It is essential to carry out experiments that rigorously exclude mono- or divalent cations when trivalent cations are the target ion species for migration. Crucibles, mortars, and boats used for the syntheses, and also the ceramic tubes for preparation should be used only for the trivalent ion conducting solid preparation. If mono- or divalent cations are included by chance, the mono- or divalent cations will appear in solids and will conduct.

By strictly obeying the above issues, multivalent ion conduction in solids has been systematically accomplished.

3. $Sc_2(WO_4)_3$-Type Solids[5–66]

The tungstates, $M_2(WO_4)_3$, which show trivalent cation conducting behavior, are known to possess two crystal structures depending on the trivalent cation size, as depicted in Figure 1.[67] One is an orthorhombic $Sc_2(WO_4)_3$ structure, and the other is a $Eu_2(WO_4)_3$-type structure with monoclinic symmetry. The $Sc_2(WO_4)_3$-type is accepted as a quasi-layered structure with a large space between the layers where M^{3+} ions can migrate, as shown in Figure 2a. In this structure, hexavalent tungsten ion (W^{6+}) binds to four oxide anions to form a rigid WO_4^{2-} tetrahedral unit, which can effectively reduce the electrostatic interaction between M^{3+} and O^{2-}, and thereby allows M^{3+} ion to diffuse in the structure. Although the $Eu_2(WO_4)_3$-type solid contains W^{6+}, the trivalent cation in the structure is surrounded by $8O^{2-}$ (M^{3+} in the $Sc_2(WO_4)_3$-type lattice has 6-fold coordination); M^{3+} cation migration is hampered because of the stronger electrostatic interaction with oxide anions (Figure 2b) compared with the $Sc_2(WO_4)_3$-type structure.

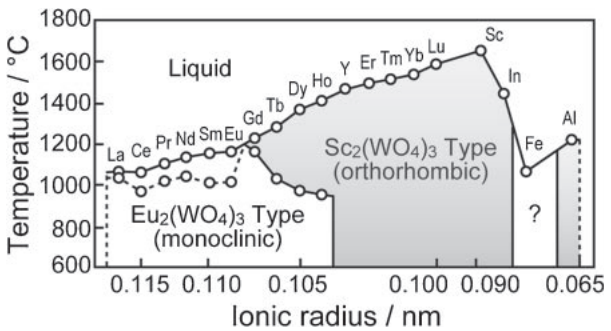

Figure 1. Phase relationships in tungstates with trivalent cations, $M_2(WO_4)_3$.

Figure 3 presents the electrical conductivities at 600 °C and activation energies for M^{3+} ion conduction in $M_2(WO_4)_3$ with the $Sc_2(WO_4)_3$-type structure.[12] Both the M^{3+} ion conductivity and the activation energy of $M_2(WO_4)_3$ drastically change with the variation of ionic radius and $Sc_2(WO_4)_3$ exhibits the highest conductivity and the lowest activation energy among the $M_2(WO_4)_3$ series. In solids with trivalent M^{3+} ions larger than Sc^{3+}, the conductivity decreases due to the comparative shrinkage of the conducting pathway. On the other hand, for Al^{3+} which has a smaller ionic radius (0.0675 nm)[68] than Sc^{3+} (0.0885 nm),[68] the conductivity is also lower, presumably due to the larger decrease in volume of the migrating trivalent ion (from Sc^{3+} to Al^{3+}) compared with that of the crystal lattice (from $Sc_2(WO_4)_3$ crystal to $Al_2(WO_4)_3$ crystal).

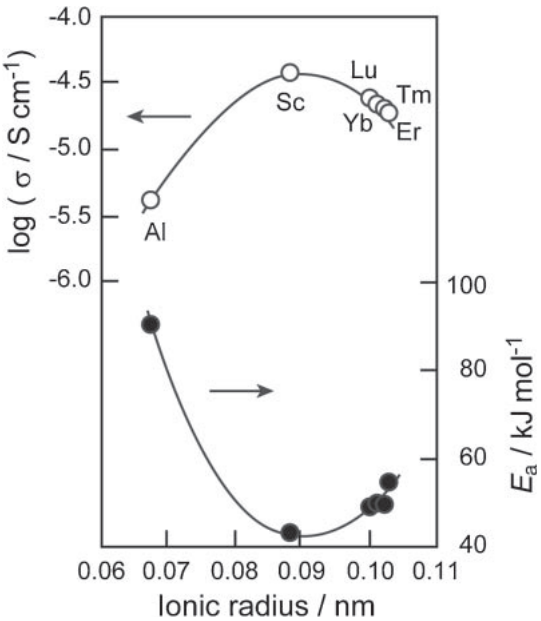

Figure 3. Electrical conductivity at 600 °C in air atmosphere, and activation energies for $M_2(WO_4)_3$ with $Sc_2(WO_4)_3$-type structure.

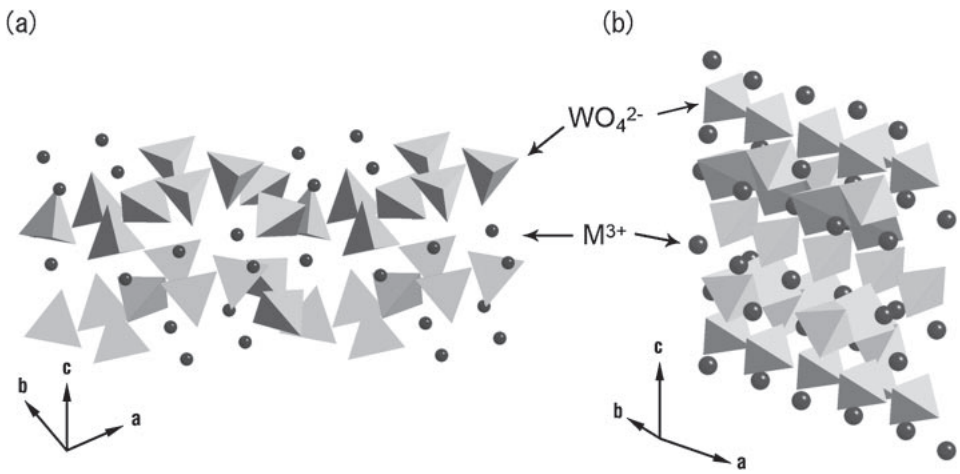

Figure 2. The crystal structures of the $M_2(WO_4)_3$-type solid for $Sc_2(WO_4)_3$-type (a) and for $Eu_2(WO_4)_3$-types (b).

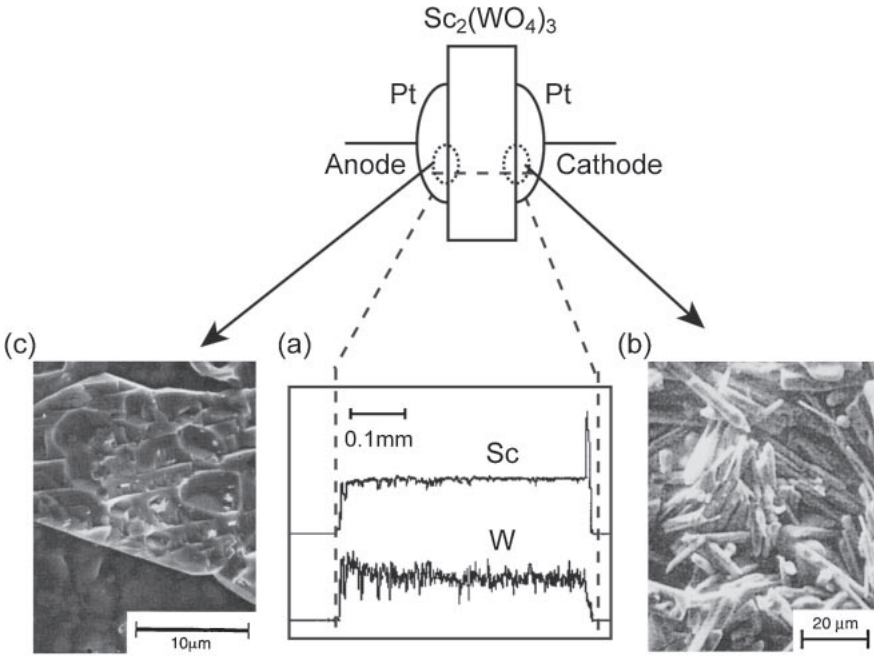

Figure 4. (a) EPMA line analysis for electrolyzed $Sc_2(WO_4)_3$ and SEM images of the (b) cathodic and (c) anodic surfaces of the electrolyzed pellet.

Trivalent M^{3+} cation conduction in the $Sc_2(WO_4)_3$-type solids was clearly demonstrated by measurements of the electrical conductivity under various oxygen pressure, polarization measurement, and DC electrolysis. From these measurements, it was clarified that the ion transference number (t_{ion}) was higher than 0.99. Furthermore, for $Sc_2(WO_4)_3$, EMF measurements of the O_2 concentration cell using $Sc_2(WO_4)_3$ were also conducted at various temperatures; the measured EMF was very close to the theoretical value calculated from the Nernst equation, which indicates that t_{ion} in the $Sc_2(WO_4)_3$ solid was estimated to be unity. Details are described in Ref. 12.

For the purpose of identifying the mobile cationic species in $Sc_2(WO_4)_3$, DC electrolysis was conducted by applying a DC voltage of 10 V, which is higher than the decomposition voltage of $Sc_2(WO_4)_3$ (ca. 1.2 V) with Pt ion-blocking electrodes. Figure 4 depicts the scanning electron microscopy (SEM) images of the cathodic and anodic surfaces, and the results of the EPMA line analysis for the $Sc_2(WO_4)_3$ solid electrolyte after the electrolysis. Needle-shaped crystallites where Sc content was 9 times higher than in the bulk $Sc_2(WO_4)_3$ were observed at the cathodic surface; these were identified as Sc_6WO_{12} by micro-area X-ray powder diffraction (XRD). On the other hand, the anodic surface change to yellow and plate-shape WO_3 was detected. These results clearly indicate that the following reaction occurred during the DC electrolysis, implying the macroscopic migration of Sc^{3+}:

$$\text{(Anodic surface)}\quad Sc_2(WO_4)_3 \rightarrow 2Sc^{3+} + 3WO_3 + (3/2)O_2 + 6e^- \quad (1)$$

[inside the sample: Sc^{3+} migrates to cathodic direction]

$$\text{(Cathodic surface)}\quad 2Sc^{3+} + 6e^- \rightarrow 2Sc \quad (2)$$

$$2Sc + (3/2)O_2 \rightarrow Sc_2O_3 \quad (3)$$

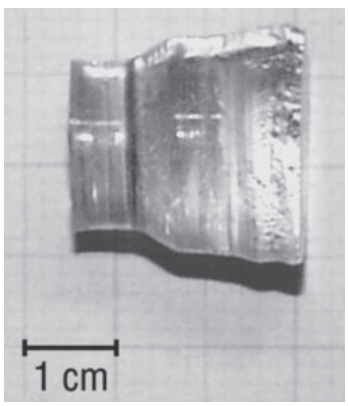

Figure 5. A photograph of the $Al_2(WO_4)_3$ single crystal grown by modified Czochralski method.

$$(8/3)Sc_2O_3 + (1/3)Sc_2(WO_4)_3 \rightarrow Sc_6WO_{12} \quad (4)$$

The detail trivalent Al^{3+} ion transport in $Al_2(WO_4)_3$ with $Sc_2(WO_4)_3$-type structure was also investigated using a large single crystal (15 mm in diameter and up to 35 mm in length) grown by a modified Czochralski (CZ) method (Figure 5).[13] Since the $Al_2(WO_4)_3$ has orthorhombic symmetry in which the Al^{3+} sites in the solid are ordered along the *b* axis, the ion conductivity behavior is considered to be anisotropic (Figure 6). From a crystallographic point of view, Al^{3+} ion should migrate easily in the *b* axis direction in the solid. It was found that the highest ion conductivity was obtained along the *b* axis, while the conductivity along the *c* axis was approximately two orders of magnitude lower as depicted in Figure 7.

To clarify the relationship between trivalent cation conductivity and the lattice volume of the tungstate, various solid solutions with $Sc_2(WO_4)_3$-type structure have also been

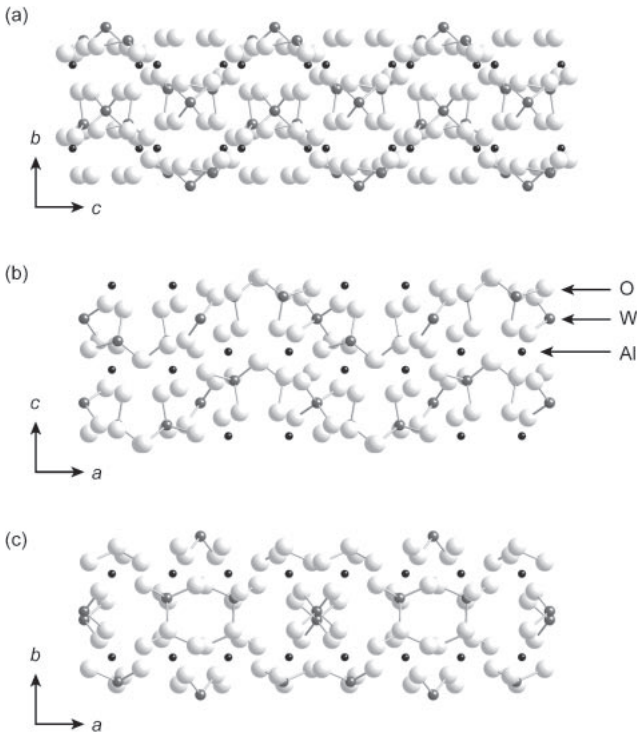

Figure 6. The $Al_2(WO_4)_3$ crystal structure viewed from each axis direction: *a* axis (a), *b* axis (b), and *c* axis (c).

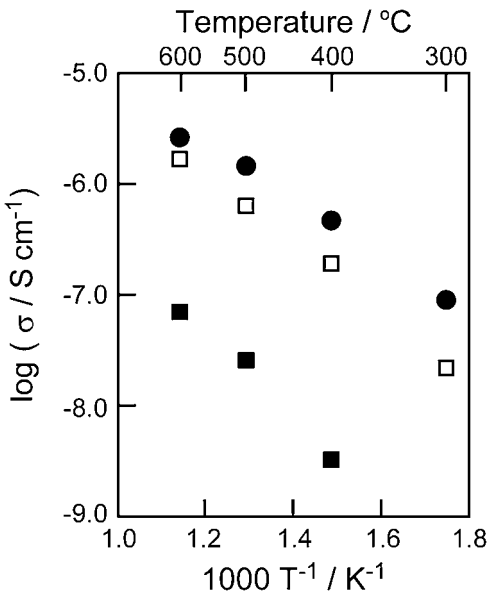

Figure 7. The Al^{3+} ion conducting properties toward each axis for the $Al_2(WO_4)_3$ single crystal (□: *a* axis, ●: *b* axis, ■: *c* axis).

extensively investigated. Figure 8 shows the electrical conductivities of $(1-x)Sc_2(WO_4)_3$–$xR_2(WO_4)_3$ (R = Gd[10] and Lu[18]) at 600 °C. For the Sc–Lu system, discontinuity in conductivity is recognized between $x = 0.5$ and 0.6. From DC electrolysis, it was clearly demonstrated that the predominant charge carriers changed from Sc^{3+} at $x < 0.5$ to Lu^{3+} at higher x ($x > 0.6$). On the other hand, the electrical conductivity of the Gd-containing system drastically decreased at around $x = 0.7$.

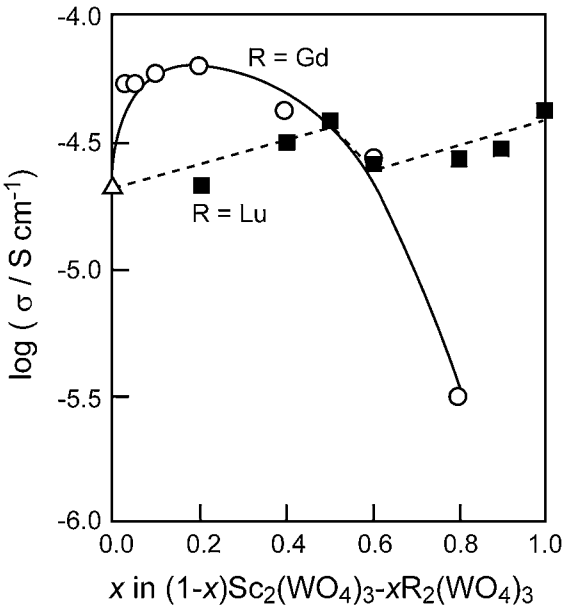

Figure 8. Electrical conductivity of $(1-x)Sc_2(WO_4)_3$–$xR_2(WO_4)_3$ (R = Lu and Gd) at 600 °C.

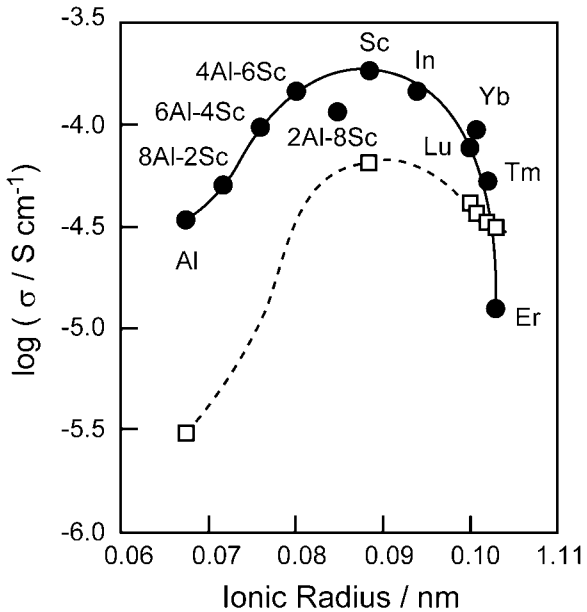

Figure 9. M^{3+} radii dependence of the electrical conductivity at 600 °C in air atmosphere for tungstates (□) and molybdates (●) with the $Sc_2(WO_4)_3$-type structure.

This decrease occurs because of the structural change from conductive $Sc_2(WO_4)_3$-type to the insulating $Eu_2(WO_4)_3$-type structure.

Trivalent cation conduction in molybdates with the same $Sc_2(WO_4)_3$-type structure, $M_2(MoO_4)_3$, was also investigated. The trivalent M^{3+} ion conductivity in molybdates was higher than that in tungstates (Figure 9) because of the smaller ionic radius of Mo^{6+} (0.055 nm)[68] than that of W^{6+} (0.056 nm),[68] resulting in smaller volume of the corresponding lattice suitable for trivalent ion conduction in the structure. Also, the strong bonding by the reduction of the bond distance between Mo^{6+} and O^{2-} contributes to the reduction of electrostatic interaction

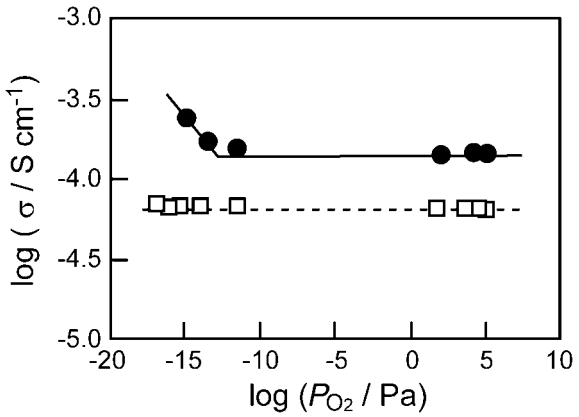

Figure 10. Oxygen partial pressure dependence of the electrical conductivity for $Sc_2(WO_4)_3$ (□) and $Sc_2(MoO_4)_3$ (●) at 700 °C.

between M^{3+} and surrounding O^{2-}. Although the $M_2(MoO_4)_3$ solids were also demonstrated to be M^{3+} ion conductors by DC electrolysis, molybdates tend to be easily reduced compared with tungstates; e.g., $Sc_2(WO_4)_3$ is still stable even at P_{O_2} of 10^{-17} Pa, while $Sc_2(MoO_4)_3$ is already reduced at $P_{O_2} = 10^{-13}$ Pa at 700 °C (Figure 10). Note that the increase in conductivity at low P_{O_2} indicates an appearance of electronic conduction caused by the reduction of Mo^{6+}.

In the case of DC electrolysis of $M_2(MoO_4)_3$, the following reactions should occur.

$$\text{(Anodic surface)}\quad M_2(MoO_4)_3 \rightarrow 2M^{3+} + 3MoO_3 + (3/2)O_2 + 6e^- \quad (5)$$

[inside the sample: M^{3+} migrates to cathode]

$$\text{(Cathodic surface)}\quad 2M^{3+} + 6e^- \rightarrow 2M \quad (6)$$

$$2M + (3/2)O_2 \rightarrow M_2O_3 \quad (7)$$

At temperatures above 750 °C where MoO_3 vaporizes in ambient atmosphere, DC electrolysis can be continued due to the appearance of fresh $M_2(MoO_4)_3$ at the anodic surface, which is quite different from tungstates; tungsten oxide (WO_3) always remains at the anodic surface during DC electrolysis, resulting in increasing electrical resistance of the sample. This unique behavior implies that continuous M_2O_3 formation can be realized at the cathodic surface. Furthermore, since we have demonstrated that Al_2O_3 deposited at the cathodic surface by the DC electrolysis of $Al_2(MoO_4)_3$ is a single crystal form, we proposed a novel technique for growing Al_2O_3 single crystals by using the DC electrolysis of the Al^{3+} ion conducting $Al_2(MoO_4)_3$ solid electrolyte.[57,58,62]

Figure 11 shows the SEM image of the cathodic surface of an $Al_2(MoO_4)_3$ pellet after DC electrolysis by applying 11 V for 3 days at 900 °C.[58] The selected area electron diffraction (SAED) pattern of a particle appearing at the cathodic surface is also inserted. The cathodic surface was covered with well-defined polyhedral particles (1.0–5.0 μm) and they were identified to be δ-Al_2O_3 from the SAED pattern. While Al_2O_3 has various metastable phases such as γ, δ, and θ, in addition to the thermodynamically stable α-Al_2O_3, it is significantly difficult to grow each phase of single crystal by

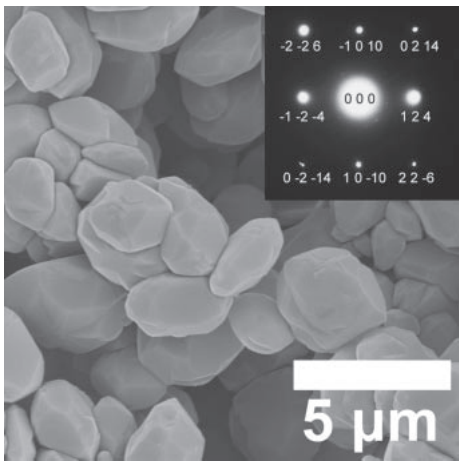

Figure 11. SEM image of the cathodic surface of the electrolyzed $Al_2(MoO_4)_3$ pellet by applying 11 V for 3 days at 900 °C. The SAED pattern of a particle is inserted.

conventional techniques because the formation temperature range of these metastable phases is very close and the intermediate phase formed depends on the particle sizes. In contrast, since the DC electrolysis method we applied can easily control the particle size by simply adjusting the electrolysis conditions, especially the operating temperature and the voltage applied, the δ-Al_2O_3 single crystal was obtained for the first time.

We also applied the same DC electrolysis method to $Tb_2(MoO_4)_3$ solid to grow single crystals of terbium oxide. Although terbium oxide (TbO_{2-x}) has various nonstoichiometric compositions such as Tb_7O_{12}, $Tb_{11}O_{20}$, $Tb_{16}O_{30}$, $Tb_{24}O_{44}$, and $Tb_{48}O_{88}$, we have succeeded in growing a single phase of $Tb_{16}O_{30}$ (11 V, 900 °C)[60] and $Tb_{24}O_{44}$ (3 V, 900 °C)[64] by adjusting the electrolysis conditions. Furthermore, this single crystal growth by DC electrolysis of $M_2(MoO_4)_3$ is also useful for other M_2O_3 solids with extremely high melting points, because the electrolysis can be carried out at moderate temperatures below 1000 °C. For Sc_2O_3 (mp: 2550 °C) and In_2O_3 (mp: 2000 °C), we successfully obtained a fine single crystal particle at as low as 950 (Sc_2O_3)[54] and 750 °C (In_2O_3),[56] respectively.

4. NASICON-Type Solid[47,69–83]

NASICON (Na^+ super ionic conductor) is a highly Na^+ conducting solid electrolyte as stated in the Introduction section, which was artificially designed by Goodenough et al. in 1976.[4] Its structure has a three-dimensional network, where PO_4 tetrahedra and ZrO_6 octahedra are linked by shared oxygen, and various solid electrolytes with the NASICON-type structure have been developed. Although Talbi et al. reported that $Ln_{1/3}Zr_2(PO_4)_3$ (Ln: lanthanoids) (The crystal structure is illustrated in Figure 12.) with the NASICON-type structure could be prepared by a sol–gel method in 1994,[84] Ln^{3+} cations in these solids are limited to several lanthanoids and their ionic conductivity has not been investigated at all. In 1999, we successfully prepared $Sc_{1/3}Zr_2(PO_4)_3$ with NASICON-type structure and investigated the Sc^{3+} transport.[69,70]

In our previous studies on the M^{3+} ion conduction in $Sc_2(WO_4)_3$-type solids, it became clear that high trivalent

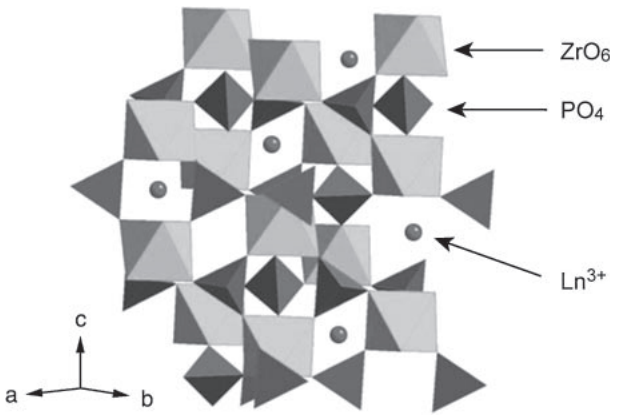

Figure 12. The crystal structure of the NASICON-type $Ln_{1/3}Zr_2(PO_4)_3$ solid.

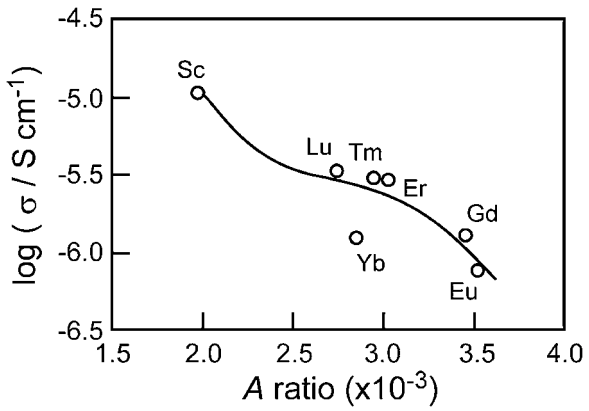

Figure 13. Relationship between the *A*-ratio and electrical conductivity at 600 °C in air atmosphere for $R_{1/3}Zr_2(PO_4)_3$ series.

cation conduction was realized by strictly controlling the lattice volume. Therefore, we introduced the concept of the mobile ion size/crystal lattice size ratio ($V_{ion}/V_{lattice}$: hereafter, we denote as *A*-ratio.) in order to optimize diffusion pathway size.[71] By investigating the *A*-ratio in $R_{1/3}Zr_2(PO_4)_3$ (R= Sc, Eu, Gd, Er, and Lu), it was found that the *A*-ratio monotonically decreased with decreasing R^{3+} radius, indicating that the R^{3+} conduction pathway expanded in this order. Since the electrostatic interaction depends on the distance between ions and their valences, the electrostatic interaction between the trivalent cation and surrounding oxide anions is stronger compared to lower valence cation if the distance M^{n+}–O^{2-} is the same. Therefore, for higher valence R^{3+}, it is important to enlarge the relative crystal lattice size to mobile R^{3+} size in order to reduce the interaction, and a high conductivity is expected for $Sc_{1/3}Zr_2(PO_4)_3$ in the $R_{1/3}Zr_2(PO_4)_3$ series. Figure 13 illustrates the *A*-ratio dependence of the electrical conductivity in $R_{1/3}Zr_2(PO_4)_3$ prepared by a sol–gel method at 600 °C.[47] As expected, $Sc_{1/3}Zr_2(PO_4)_3$ shows the highest conductivity; the DC electrolysis demonstrated Sc^{3+} ion transport in $Sc_{1/3}Zr_2(PO_4)_3$, similar to $Sc_2(WO_4)_3$.

The Al^{3+} ion is considered to be a more suitable trivalent cation species in NASICON-type phases because of the smaller ionic radius of Al^{3+} (0.0675 nm)[68] than Sc^{3+} (0.0885 nm),[68]

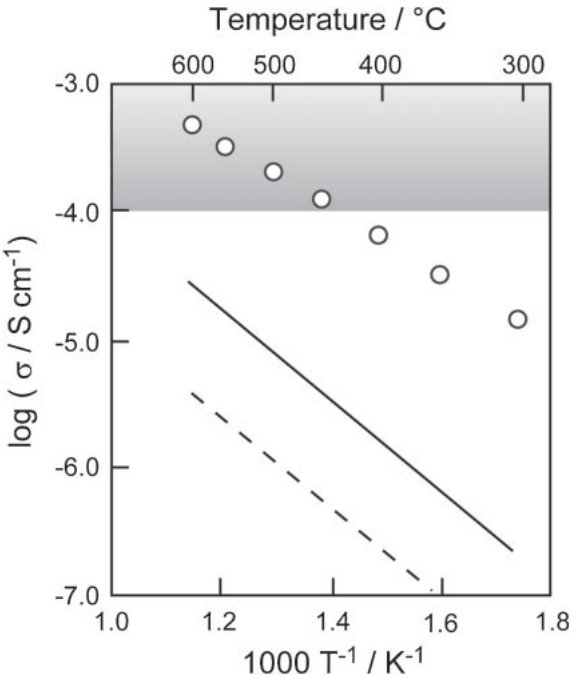

Figure 14. Temperature dependence of the Al^{3+} ion conductivity of $(Al_{0.2}Zr_{0.8})_{20/19}Nb(PO_4)_3$ (○) and the corresponding data of $Al_2(WO_4)_3$ with the $Sc_2(WO_4)_3$-type structure (- - -). The Sc^{3+} ion conductivity of $Sc_{1/3}Zr_2(PO_4)_3$ (—) is also shown.

expecting a smaller *A*-ratio for $Al_{1/3}Zr_2(PO_4)_3$. However, the $Al_{1/3}Zr_2(PO_4)_3$ solid cannot be obtained due to stereological limitations. In order to realize the formation of NASICON-type structure with the target Al^{3+} ion, smaller lattice size is required for the solid. In 2002, we prepared $(Al_xZr_{1-x})_{4/(4-x)}Nb(PO_4)_3$ solids[75] in which the NASICON-type lattice was successfully shrunk by partially substituting the Zr^{4+} (0.086 nm)[68] sites with smaller pentavalent Nb^{5+} (0.078 nm).[68] In addition, the higher valence state of Nb^{5+} than Zr^{4+} leads to effective reduction of electrostatic interaction between Al^{3+} ions and O^{2-} anions and also contributes to the enhancement of the bonding between Nb^{5+} and O^{2-}, resulting in the improvement of the thermal stability (even at 1200 °C) of the $(Al_xZr_{1-x})_{4/(4-x)}Nb(PO_4)_3$ solids. Among the $(Al_xZr_{1-x})_{4/(4-x)}Nb(PO_4)_3$ series, only samples with $x \leq 0.2$ could form a single phase with the NASICON-type structure; the highest Al^{3+} ion conductivity was obtained for the solubility limit composition of $(Al_{0.2}Zr_{0.8})_{20/19}Nb(PO_4)_3$. Figure 14 displays the trivalent Al^{3+} ion conductivity of the $(Al_{0.2}Zr_{0.8})_{20/19}Nb(PO_4)_3$ solid and the corresponding data for $Al_2(WO_4)_3$ and $Sc_{1/3}Zr_2(PO_4)_3$. The trivalent ionic conductivity (4.5×10^{-4} S cm^{-1} at 600 °C) of $(Al_{0.2}Zr_{0.8})_{20/19}Nb(PO_4)_3$ is two orders of magnitude higher than that of $Al_2(WO_4)_3$; its value reaches the practical application range of $\sigma > 10^{-4}$ S cm^{-1} (shaded area in Figure 14).

This suggests that there is a suitable crystal lattice size for each trivalent cation species and the crystal lattice can be obtained by the partial replacement of constituent ions in the NASICON-type compounds. The suitable sizes for rare earth ion conduction were also extensively investigated for $(R_{0.05}Zr_{0.95})_{80/79}Nb(PO_4)_3$ by introducing an *A*-ratio similar to those for the $R_{1/3}Zr_2(PO_4)_3$ series.[83] Figure 15 shows R^{3+} ionic

radius dependence of the *A*-ratio for the $(R_{0.05}Zr_{0.95})_{80/79}$-$Nb(PO_4)_3$ series. The *A*-ratios monotonically decrease with reducing the trivalent ionic radius, and the values are almost the same as those for $R_{1/3}Zr_2(PO_4)_3$ which is depicted as a dashed line in the same figure, indicating that similar lattice volume change occurs for both series by changing the R^{3+} ionic size. These phenomena appear by the countervailing effect of the lattice shrinkage by substituting the Zr^{4+} (0.086 nm; 6-coordinate)[68] site with smaller Nb^{5+} (0.078 nm; 6-coordinate)[68] in the solids and the lattice expansion due to the decrease of R–O bonding that is caused by the reduction of R^{3+} cation concentration. Figure 16 depicts the *A*-ratio dependencies of the trivalent R^{3+} conductivity at 600 °C and the activation energy for R^{3+} migration in $(R_{0.05}Zr_{0.95})_{80/79}Nb(PO_4)_3$ and $R_{1/3}Zr_2(PO_4)_3$. Since the $(Dy_{0.05}Zr_{0.95})_{80/79}Nb(PO_4)_3$ solid possesses both the highest ion conductivity and the lowest activation energy in the $(R_{0.05}Zr_{0.95})_{80/79}Nb(PO_4)_3$ series, the Dy^{3+} ion is in such a circumstance to migrate most smoothly in solids. This also supports the idea that the optimum ion conducting pathway in the $(R_{0.05}Zr_{0.95})_{80/79}Nb(PO_4)_3$ series was obtained for R = Dy. Although in the case for $R_{1/3}Zr_2(PO_4)_3$, the highest trivalent ion conductivity was obtained for the smallest Sc^{3+} due to the small bottleneck which is caused by the strong R–O bonding in the structure, R–O bonding in the $(R_{0.05}Zr_{0.95})_{80/79}Nb(PO_4)_3$ solids should be weakened by introducing the pentavalent Nb^{5+} into the structure. As a result, a suitable lattice size for R^{3+} migration was successfully obtained for R = Dy in the $(R_{0.05}Zr_{0.95})_{80/79}Nb(PO_4)_3$ series, whose ionic radius is larger than Sc^{3+}.

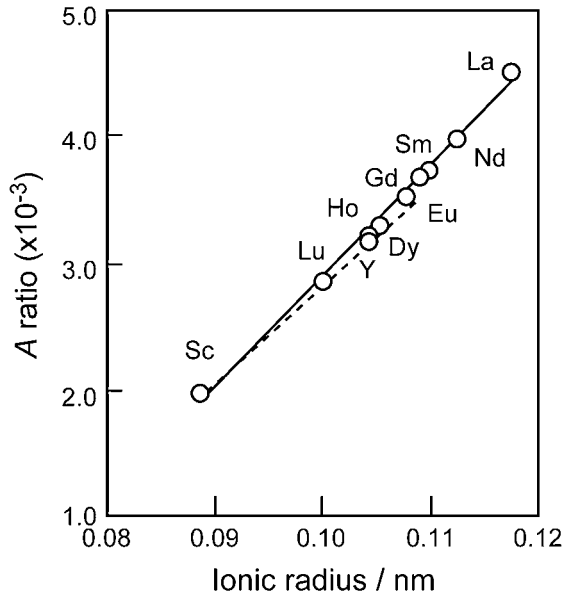

Figure 15. R^{3+} ionic radius dependence of the *A*-ratio for $(R_{0.05}Zr_{0.95})_{80/79}Nb(PO_4)_3$ (—) and $R_{1/3}Zr_2(PO_4)_3$ solids (- - -).

5. Conclusion

We have been investigating trivalent cation conduction in rigid crystal lattices since 1995, and have successfully developed various trivalent cation conducting solid electrolytes from the above-mentioned strategies.

For $Sc_2(WO_4)_3$-type solids with quasi-layered two-dimensional structure, we have successfully demonstrated trivalent cation conduction in solid for the first time, and anisotropic ion migration behavior has also been demonstrated by using an $Al_2(WO_4)_3$ single crystal which was grown by a modified Czochralski method. Furthermore, we have also successfully grown single crystals of δ-Al_2O_3, nonstoichiometric TbO_{2-x}, and high-melting compounds of Sc_2O_3 and In_2O_3 by a novel DC electrolysis method under moderate conditions. These phenomena explicitly indicate the macroscopic trivalent ion migration in the solids.

For the three-dimensional NASICON-type solids, we have clearly demonstrated the relationship between the trivalent R^{3+} ion conductivity and the lattice volume of the NASICON-type

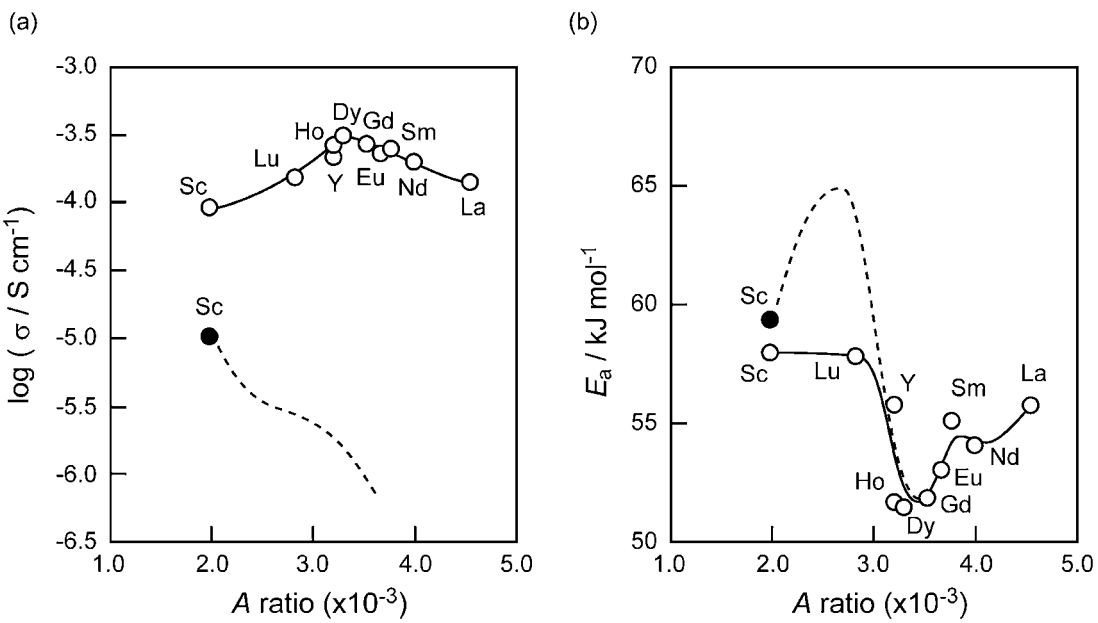

Figure 16. The relationships between the *A*-ratio and the conductivity at 600 °C (a) and between the *A*-ratio and the activation energy (b) for the $(R_{0.05}Zr_{0.95})_{80/79}Nb(PO_4)_3$ (—) and the $R_{1/3}Zr_2(PO_4)_3$ solids (- - -).

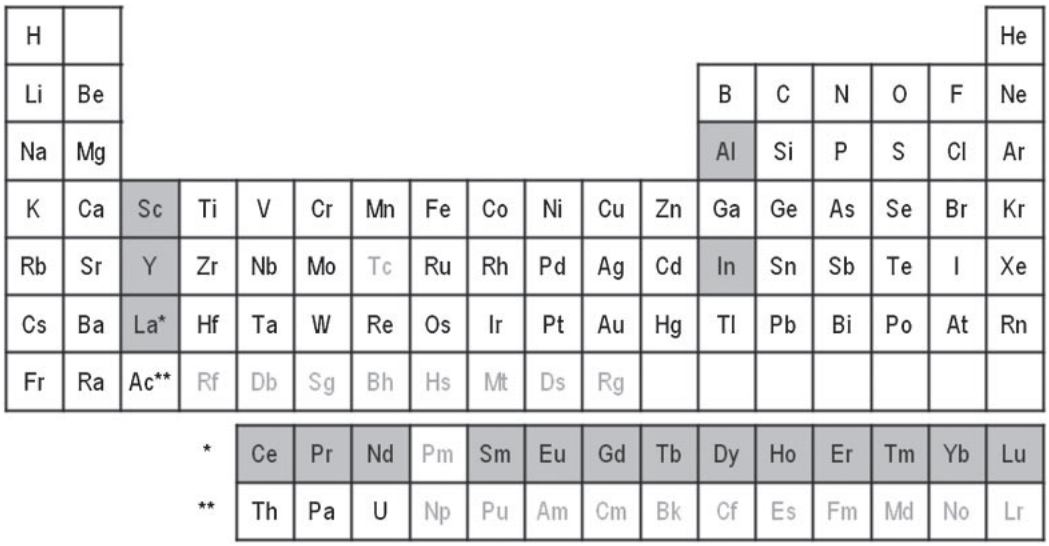

Figure 17. Trivalent cation species demonstrated to migrate in solids.

structure by introducing the concept of *A*-ratio ($V_{ion}/V_{lattice}$). In the NASICON-type trivalent cation conductors, we have succeeded in developing the Al^{3+} ion conducting solid, $(Al_{0.2}Zr_{0.8})_{20/19}Nb(PO_4)_3$, whose trivalent Al^{3+} ion conductivity enters a practically applicable range of $>10^{-4}\,S\,cm^{-1}$ above 600 °C.

From our continuous investigations on trivalent cation conducting solids, at present, it is clarified that 18 trivalent cations join the migrating ion group in solids in addition to the well-known mono- and divalent ions (highlighted in Figure 17).

6. Experimental

6.1 Sample Preparation. $M_2(WO_4)_3$ (M = Al, In, Sc, Er, Tm, Yb, and Lu) were prepared by conventional solid-state reaction. A stoichiometric amount of $Al(OH)_3$ or R_2O_3 (R = Sc, Er, Tm, Yb, and Lu) and WO_3 was mixed in a mortar and the mixture was calcined at 1000 °C for 12 h in air. Then, the sample was calcined repeatedly at 1200–1400 °C for 12 h in air until a single phase of the $Sc_2(WO_4)_3$-type structure was obtained. The resulting powder was made into pellets and sintered at 1200–1400 °C for 12 h in air. For the heavy rare earths, Er–Lu, the sample powders were dried in vacuum at 100–150 °C before sintering due to their hygroscopic nature.

$M_2(MoO_4)_3$ (M = Al, In, Sc, Er, Tm, Yb, and Lu) was synthesized by heating a stoichiometric mixture of $Al(OH)_3$ or R_2O_3 (R = Sc, Er, Tm, Yb, and Lu) and MoO_3 at 700–1000 °C for 6–12 h in air. The calcined powder was ground and reheated at 800–1100 °C for 12 h in air several times. For the heavy rare earths, Er–Lu, the sample powders were dried before sintering the same as the tungstates.

Single crystals of $Al_2(WO_4)_3$ were grown from reagent grade Al_2O_3 and WO_3 by the Czochralski method.[20] The axis directions and lattice parameters were determined by using a four-circle single-crystal diffractometer. For the electrical conductivity measurements, the single crystals were cut into a cylinder shape with the cylinder axes parallel to *a*-, *b*-, and *c*-axes.

NASICON-type $R_{1/3}Zr_2(PO_4)_3$ (R = Sc, Eu, Gd, Er, and Lu) was prepared by a sol–gel method. R_2O_3 and $ZrO(NO_3)_2 \cdot 2H_2O$ were separately dissolved in nitric acid solution (3 M), then the solutions were mixed together. By adding the $(NH_4)_2HPO_4$ solution (3%) into mixed nitric acid solution, precipitations were obtained. The precipitations were dried 130 °C for 6 h, and then the powders were calcined at 850 °C for 12 h in air. The sample powder obtained was pelletized and sintered at 850 °C for 12 h in air.

$(M_xZr_{1-x})_{4/(4-x)}Nb(PO_4)_3$ series with NASICON-type structure were obtained by ball milling. Appropriate amount of starting materials, $Al(OH)_3$ or R_2O_3 (R = Sc, Y, La, Nd, Sm, Eu, Gd, Dy, Ho, and Lu), ZrO_2, Nb_2O_5, and $(NH_4)_2HPO_4$, were mixed in an agate mortar at a rotation speed of 300 rpm for 6 h. The samples obtained were calcined at 1000 °C for 12 h in air. Then, the sample was calcined at 1000–1300 °C for 12 h in air several times. After grinding the sample obtained, the sample powder was made into pellets and sintered at 1000–1300 °C for 12 h in air.

The sample identification was conducted by X-ray powder diffraction (XRD) with Cu Kα radiation.

6.2 Electrical Conductivity Measurements. AC conductivity of samples were measured by complex impedance in various atmospheres with oxygen pressure controlled by using O_2, synthetic air, N_2, He, and CO–CO_2 mixtures. The DC conductivity measurement of the sample was carried out by monitoring the voltage generated by passing a constant current of 0.1 μA into the sample.

DC electrolysis (including the single crystal growth by using $M_2(MoO_4)_3$) of the sample was conducted by applying a DC voltage to the sample which was sandwiched by Pt plate electrodes. The DC voltage applied for the sample was higher than the decomposition voltage of the sample which was directly determined by the preliminary investigation of the *I–V* relationship. After DC electrolysis, the sample was investigated by XRD, scanning electron microscopy (SEM), and electron probe micro analysis (EPMA).

References

1 E. Warburg, F. Tegetmeier, *Wiedemann Ann. Phys.* **1988**, *32*, 455.

2 C. Wagner, *Naturwissenschaften* **1943**, *31*, 265.
3 C. Tubandt, *Z. Anorg. Allg. Chem.* **1921**, *115*, 105.
4 J. B. Goodenough, H. Y.-P. Hong, J. A. Kafalas, *Mater. Res. Bull.* **1976**, *11*, 203.
5 Y. Kobayashi, N. Imanaka, G. Adachi, *J. Cryst. Growth* **1994**, *143*, 362.
6 N. Imanaka, Y. Kobayashi, G. Adachi, *Chem. Lett.* **1995**, 433.
7 Y. Kobayashi, T. Egawa, S. Tamura, N. Imanaka, G. Adachi, *Chem. Mater.* **1997**, *9*, 1649.
8 G. Adachi, N. Imanaka, *J. Alloys Compd.* **1997**, *250*, 492.
9 N. Imanaka, Y. Kobayashi, S. Tamura, G. Adachi, *Electrochem. Solid-State Lett.* **1998**, *1*, 271.
10 Y. Kobayashi, T. Egawa, Y. Okazaki, S. Tamura, N. Imanaka, G. Adachi, *Solid State Ionics* **1998**, *111*, 59.
11 S. Tamura, T. Egawa, Y. Okazaki, Y. Kobayashi, N. Imanaka, G. Adachi, *Chem. Mater.* **1998**, *10*, 1958.
12 N. Imanaka, Y. Kobayashi, K. Fujiwara, T. Asano, Y. Okazaki, G. Adachi, *Chem. Mater.* **1998**, *10*, 2006.
13 N. Imanaka, S. Tamura, M. Hiraiwa, G. Adachi, H. Dabkowska, A. Dabkowski, J. E. Greedan, *Chem. Mater.* **1998**, *10*, 2542.
14 J. Köhler, N. Imanaka, G. Adachi, *Chem. Mater.* **1998**, *10*, 3790.
15 N. Imanaka, G. Adachi, *Molten Salts* **1998**, *41*, 177.
16 Y. Kobayashi, S. Tamura, N. Imanaka, G. Adachi, *Solid State Ionics* **1998**, *113–115*, 545.
17 J. Köhler, Y. Kobayashi, N. Imanaka, G. Adachi, *Solid State Ionics* **1998**, *113–115*, 553.
18 Y. Kobayashi, T. Egawa, S. Tamura, N. Imanaka, G. Adachi, *Solid State Ionics* **1999**, *118*, 325.
19 S. Tamura, N. Imanaka, G. Adachi, *Adv. Mater.* **1999**, *11*, 64.
20 A. Dabkowski, H. A. Dabkowska, J. E. Greedan, G. Adachi, Y. Kobayashi, S. Tamura, M. Hiraiwa, N. Imanaka, *J. Cryst. Growth* **1999**, *197*, 879.
21 N. Imanaka, M. Hiraiwa, S. Tamura, G. Adachi, H. Dabkowska, A. Dabkowski, *J. Cryst. Growth* **1999**, *200*, 169.
22 J. Köhler, N. Imanaka, G. Adachi, *J. Mater. Chem.* **1999**, *9*, 1357.
23 J. Köhler, N. Imanaka, G. Adachi, *Solid State Ionics* **1999**, *122*, 173.
24 N. Imanaka, T. Asano, S. Tamura, Y. Kobayashi, G. Adachi, *Electrochem. Solid-State Lett.* **1999**, *2*, 330.
25 G. Adachi, J. Köhler, N. Imanaka, *Electrochemistry* **1999**, *67*, 744.
26 N. Imanaka, Y. Okazaki, Y. Kobayashi, S. Tamura, T. Asano, T. Egawa, G. Adachi, *Solid State Ionics* **1999**, *126*, 41.
27 N. Imanaka, J. Köhler, G. Adachi, *Electrochem. Solid-State Lett.* **1999**, *2*, 556.
28 J. Köhler, N. Imanaka, G. Adachi, *Z. Anorg. Allg. Chem.* **1999**, *625*, 1890.
29 N. Imanaka, M. Hiraiwa, S. Tamura, G. Adachi, *Electrochem. Solid-State Lett.* **1999**, *2*, 570.
30 N. Imanaka, M. Hiraiwa, S. Tamura, G. Adachi, H. Dabkowska, A. Dabkowski, *J. Cryst. Growth* **2000**, *209*, 217.
31 N. Imanaka, M. Hiraiwa, S. Tamura, G. Adachi, H. Dabkowska, A. Dabkowski, *J. Cryst. Growth* **2000**, *208*, 466.
32 N. Imanaka, J. Köhler, T. Masui, G. Adachi, E. Taguchi, H. Mori, *J. Am. Ceram. Soc.* **2000**, *83*, 427.
33 N. Imanaka, Y. Kobayashi, S. Tamura, G. Adachi, *Solid State Ionics* **2000**, *136–137*, 319.
34 M. Hiraiwa, S. Tamura, N. Imanaka, G. Adachi, H. Dabkowska, A. Dabkowski, *Solid State Ionics* **2000**, *136–137*, 427.
35 N. Imanaka, S. Tamura, G. Adachi, Y. Kowada, *Solid State Ionics* **2000**, *130*, 179.
36 N. Imanaka, S. Tamura, Y. Kobayashi, Y. Okazaki, M. Hiraiwa, T. Ueda, G. Adachi, *J. Alloys Compd.* **2000**, *303–304*, 303.
37 J. Köhler, N. Imanaka, G. Adachi, *Solid State Ionics* **2000**, *136–137*, 431.
38 Y. Okazaki, T. Ueda, S. Tamura, N. Imanaka, G. Adachi, *Solid State Ionics* **2000**, *136–137*, 437.
39 N. Imanaka, T. Ueda, Y. Okazaki, S. Tamura, G. Adachi, *Chem. Mater.* **2000**, *12*, 1910.
40 N. Imanaka, M. Hiraiwa, G. Adachi, *J. Cryst. Growth* **2000**, *220*, 176.
41 G. Adachi, N. Imanaka, S. Tamura, *J. Alloys Compd.* **2001**, *323–324*, 534.
42 R. A. Secco, H. Liu, N. Imanaka, G. Adachi, *J. Mater. Sci. Lett.* **2001**, *20*, 1339.
43 N. Imanaka, S. Tamura, G. Adachi, *Electrochemistry* **2001**, *69*, 802.
44 R. A. Secco, H. Liu, N. Imanaka, G. Adachi, M. D. Rutter, *J. Phys. Chem. Solids* **2002**, *63*, 425.
45 N. Imanaka, J. Köhler, S. Tamura, G. Adachi, *Eur. J. Inorg. Chem.* **2002**, 105.
46 H. Liu, R. A. Secco, N. Imanaka, G. Adachi, *Solid State Commun.* **2002**, *121*, 177.
47 N. Imanaka, G. Adachi, *J. Alloys Compd.* **2002**, *344*, 137.
48 N. Imanaka, M. Hiraiwa, S. Tamura, G. Adachi, H. Dabkowska, A. Dabkowski, *Mater. Lett.* **2002**, *55*, 93.
49 G. Adachi, N. Imanaka, S. Tamura, *Chem. Rev.* **2002**, *102*, 2405.
50 N. Imanaka, S. Yoshikawa, M. Hiraiwa, S. Tamura, G. Adachi, *Mater. Lett.* **2002**, *56*, 856.
51 N. Imanaka, M. Hiraiwa, S. Tamura, G. Adachi, H. Dabkowska, A. Dabkowski, *J. Mater. Sci.* **2002**, *37*, 3483.
52 R. A. Secco, H. Liu, N. Imanaka, G. Adachi, *J. Phys.: Condens. Matter* **2002**, *14*, 11285.
53 H. Liu, R. A. Secco, N. Imanaka, M. D. Rutter, G. Adachi, T. Uchida, *J. Phys. Chem. Solids* **2003**, *64*, 287.
54 N. Imanaka, Y. W. Kim, T. Masui, G. Adachi, *Cryst. Growth Des.* **2003**, *3*, 289.
55 T. Masui, Y. W. Kim, N. Imanaka, G. Adachi, *J. Alloys Compd.* **2004**, *374*, 97.
56 N. Imanaka, T. Masui, Y. W. Kim, G. Adachi, *J. Cryst. Growth* **2004**, *264*, 134.
57 N. Imanaka, Y. W. Kim, T. Masui, T. Sakata, H. Mori, *Electrochemistry* **2004**, *72*, 405.
58 N. Imanaka, T. Masui, Y. W. Kim, *Cryst. Growth Des.* **2004**, *4*, 663.
59 T. Masui, Y. W. Kim, N. Imanaka, *Solid State Ionics* **2004**, *174*, 67.
60 N. Imanaka, T. Masui, Y. W. Kim, *J. Solid State Chem.* **2004**, *177*, 3839.
61 N. Imanaka, Y. Hasegawa, I. Hasegawa, *Ionics* **2004**, *10*, 385.
62 S. Tamura, Y.-W. Kim, T. Masui, N. Imanaka, *Solid State Ionics* **2004**, *173*, 131.
63 N. Imanaka, *J. Ceram. Soc. Jpn.* **2005**, *113*, 387.
64 S. Isota, T. Masui, S. Tamura, N. Imanaka, *J. Alloys Compd.* **2006**, *418*, 101.

65 S. Isota, T. Masui, S. Tamura, N. Imanaka, *J. Alloys Compd.* **2008**, *451*, 644.
66 T. Masui, S. Isota, S. Tamura, N. Imanaka, *Cryst. Growth Des.* **2008**, *8*, 1035.
67 K. Nassau, J. W. Shiever, E. T. Keve, *J. Solid State Chem.* **1971**, *3*, 411.
68 R. D. Shannon, *Acta Crystallogr., Sect. A* **1976**, *32*, 751.
69 S. Tamura, N. Imanaka, G. Adachi, *Adv. Mater.* **1999**, *11*, 1521.
70 S. Tamura, N. Imanaka, G. Adachi, *Solid State Ionics* **2000**, *136–137*, 423.
71 S. Tamura, N. Imanaka, G. Adachi, *J. Alloys Compd.* **2001**, *323–324*, 540.
72 S. Tamura, N. Imanaka, G. Adachi, *Chem. Lett.* **2001**, 672.
73 S. Tamura, N. Imanaka, G. Adachi, *J. Mater. Sci. Lett.* **2001**, *20*, 2123.
74 S. Tamura, N. Imanaka, G. Adachi, *Solid State Ionics* **2002**, *154–155*, 767.
75 N. Imanaka, Y. Hasegawa, M. Yamaguchi, M. Itaya, S. Tamura, G. Adachi, *Chem. Mater.* **2002**, *14*, 4481.
76 Y. Hasegawa, N. Imanaka, G. Adachi, *J. Solid State Chem.* **2003**, *171*, 387.
77 Y. Hasegawa, S. Tamura, N. Imanaka, G. Adachi, *J. Alloys Compd.* **2004**, *379*, 262.
78 Y. Hasegawa, N. Imanaka, *Solid State Ionics* **2005**, *176*, 2499.
79 Y. Hasegawa, S. Tamura, N. Imanaka, *J. New Mater. Electrochem. Syst.* **2005**, *8*, 203.
80 Y. Hasegawa, N. Imanaka, *J. Alloys Compd.* **2006**, *408–412*, 661.
81 Y. Hasegawa, T. Hoshiyama, S. Tamura, N. Imanaka, *J. New Mater. Electrochem. Syst.* **2007**, *10*, 177.
82 S. Tamura, S. Yamamoto, N. Imanaka, *J. New Mater. Electrochem. Syst.* **2008**, *11*, 1.
83 Y. Hasegawa, S. Tamura, M. Sato, N. Imanaka, *Bull. Chem. Soc. Jpn.* **2008**, *81*, 521.
84 M. A. Talbi, R. Brochu, C. Parent, L. Rabardel, G. Le Flem, *J. Solid State Chem.* **1994**, *110*, 350.

Award recipient

Nobuhito Imanaka earned his B.E. (1981) and M.E. (1983) degrees in Applied Chemistry from Osaka University. He then obtained a Ph.D. degree from Osaka University in 1986. He has joined the faculty at Osaka University since 1988 and at present he is Full Professor. He also contributes as the President of The Rare Earth Society of Japan. His main research fields include rare earths and functional materials such as solid electrolytes and chemical sensors. He has received various awards. For example, Ichimura Science Award in 2005, Inoue Science Award in 2008, Yazaki Science Award in 2009, and The Chemical Society of Japan Award for Creative Work for 2009.

Shinji Tamura was born in Osaka, Japan in 1972. He received his B.E. (1997) degree in Applied Chemistry from Osaka University. He then obtained his M.E. (1999) and Ph.D. (2001) degree from Osaka University. He has joined the faculty at Osaka University since 2001 and he is Assistant Professor. His main research fields are the solid electrolytes and chemical sensors.